Multicationic Sr4Mn3O10 mesostructures: molten salt synthesis, analytical electron microscopy study and reactivity

Irma N González-Jiménez, Almudena Torres-Pardo, Simon Rano, Christel Laberty-Robert, Juan Carlos Hernández-Garrido, Miguel Lopez-Haro, José J Calvino, Aurea Varela, Clément Sanchez, Marina Parras, et al.

Multicationic $Sr_4Mn_3O_{10}$ mesostructures: molten salt synthesis, analytical electron microscopy study and reactivity

Irma N. González-Jiménez,[a] Almudena Torres-Pardo,[a,b] Simon Rano,[c] Christel Laberty-Robert,[c] Juan Carlos Hernández-Garrido,[d,e] Miguel López-Haro,[d,e] José J. Calvino,[d,e] Áurea Varela,[a] Clément Sanchez,[c] Marina Parras,[a,*] José M. González-Calbet,[a,f] David Portehault[c,*]

[a.] *Departamento de Química Inorgánica, Facultad de CC. Químicas, Universidad Complutense de Madrid, 28040 Madrid, Spain,E-mail: mparras@quim.ucm.es*

[b.] *CEI Campus Moncloa, UCM-UPM, Madrid, Spain.*

[c.] *Sorbonne Université, CNRS, Collège de France, Laboratoire Chimie de la Matière Condensée de Paris, LCMCP, 4 Place Jussieu, F-75005 Paris, France. E-mail: david.portehault@sorbonne-universite.fr*

[d.] *Departamento de Ciencia de los Materiales e Ingeniería Metalúrgica y Química Inorgánica, Facultad de Ciencias, Universidad de Cádiz, Campus Río San Pedro S/N, Puerto Real 11510 (Cádiz), Spain.*

[e.] *Instituto Universitario de Investigación de Microscopía Electrónica y Materiales (IMEYMAT). Facultad de Ciencias. Universidad de Cádiz. Campus Río San pedro S/N, Puerto Real 11510 (Cádiz), Spain.*

[f.] *Centro Nacional de Microscopía Electrónica, Universidad Complutense, 28040 Madrid, Spain.*

Electronic Supplementary Information (ESI) available: Experimental procedures, including synthesis, characterization methods, Figures S1-S11, Table S1 and Movies S1 and S2.

Inorganic molten salts offer opportunities for room pressure liquid-phase synthesis of materials in the temperature range approx. 300-1000 °C unreachable by common solvents. Hence, they have been used for flux synthesis of large single crystals and more recently for producing nano- and meso-particles of metal oxides and other non-oxides whose crystallization occurs at these temperatures. However, the nanoscale and mesoscale oxide particles obtained up-to-now by molten salt synthesis were constituted of phases that had previously been reported as nano- and meso-particles by other fabrication methods. Hence, the potential of molten salts to trigger the formation of unreported oxide nano- and meso-structures has not been demonstrated, thus questioning their suitability as a new platform for the synthesis of new nano- and meso-structures. Herein, we report the first occurrence of mesoplatelets of a complex manganese oxide, thus showing that molten salts provide a realm of opportunities to design complex oxides at the mesoscale. We thus pave the way to particle shapes and structures that can only be reached in molten salts.

Inorganic molten salts are known as fluxes for the synthesis of novel bulk inorganic compounds and of mesostructures and nanostructures with crystal habits different from those observed in more conventional solvents. However, they have not demonstrated the ability to provide mesostructures and nanostructures of complex metal oxides that are currently unreported at the mesoscale and nanoscale. In this report we show the first occurrence of $Sr_4Mn_3O_{10}$ at the mesoscale, as platelets synthesized in molten strontium hydroxide at 600 °C with basal face of few hundreds of nanometers and thicknesses ranging from 20 to 100 nm. We address carefully the atom-scale structure by transmission electron microscopy, including electron energy loss spectroscopy and electron tomography. We then propose that the final morphology is driven by the surface charge of each facet through surface energy. The reactivity of these platelets is then addressed, highlighting cation leaching in contact with acidic water, which results in crystalline-amorphous core-shell platelets that are active electrocatalysts towards the oxygen reduction reaction.

Introduction

Synthesis in high temperature inorganic molten salts (HTIMS) is known since decades for its relevance in the production of high quality crystals for a wide range of inorganic materials from oxides, chalcogenides, metals, to metal-free covalent organic frameworks.[1] During the last years, these flux syntheses have been in turn rerouted to target materials at the nanoscale and mesoscale, with dimensions below 100 nm and from 100 nm to submicrons, respectively. Such efforts have been mainly driven by the improved crystallinity provided by such synthesis routes.[2–4] It is however striking how molten salt-mediated syntheses of nanoscaled and mesoscaled materials are currently bound to compounds that had been already reported at the nanoscale. Indeed, the most remarkable results of morphology control through molten salt media relate to the exposure of high energy facets that are difficult to obtain by other ways,[1] for instance for nano- or meso-particles of wurtzite ZnO,[5] rock-salt MgO,[5] spinels Co_3O_4[5] and $ZnFe_2O_4$,[5] rutile SnO_2[1,5,6] and aluminosilicate mullite.[7] All these examples deal with compounds that have been obtained at the nano- and meso-scales by other solution-mediated ways, which are very often simpler to implement than molten salt syntheses.[8,9] Actually, there are very few cases where HTIMS provide access to the first occurrence of nano- and meso-structures for a given material: some metal borides,[10–12] some silicides[13] and boron carbon nitrides[14] are the only

examples to our knowledge. Especially, no evidence has been provided than HTIMS are relevant to target new nano- and/or meso-scaled metal oxides, in the sense of oxide compounds not previously reported at the nano/meso-scale. A first demonstration of the ability of HTIMS to provide nano/meso-structures for complex oxides known only as particles larger than micrometers ("bulk phases") could not only validate further the high utility of molten salt synthesis, but also act as a stepping stone for the community aiming at new functional nano/mesostructure design, by unveiling a poorly known synthetic tool for nanosciences.

Herein we develop a molten salt synthesis of a multicationic strontium manganese oxide $Sr_4Mn_3O_{10}$. Manganese-based oxides are a nice playground to assess the possibility of phase selective synthesis at the nanoscale, as they exhibit large structural diversity.[15] Especially, the synthesis of $Sr_4Mn_3O_{10}$ was reported only above 900 °C and always in the bulk state.[16–19] To reach the nanoscale, the synthesis temperature should be decreased, which could result in turn in detrimental kinetic stabilization of many intermediate solids.[15] Besides, the properties of $Sr_4Mn_3O_{10}$ are mostly unreported, except magnetic properties.[16–19] Overall, $Sr_4Mn_3O_{10}$ is then an interesting case-study for using molten salts to access new nanostructures. We use state-of-the-art scanning transmission electron microscopy (STEM) to yield direct chemical information down to the atomic scale with low dose by analytical STEM.[20–23] We also assess precisely the unusual mesoscale morphology by electron tomography. We then discuss the peculiar crystal habit by focusing on the local structure of the crystal facets in contact with the molten salt. We finally provide first insights into the reactivity and electrocatalytic properties of this new mesoscale material.

Results and discussion

$Sr_4Mn_3O_{10}$ platelets were synthesized under argon for 72 h, from potassium permanganate, the manganese precursor, and liquid strontium hydroxide $Sr(OH)_2$, the Sr source and the solvent. In its solid form $Sr(OH)_2$ is a fully ionic compound showing complete charge transfer and ionization into Sr^{2+} cations and OH^- anions.[24] $Sr(OH)_2$ is then a solid salt. Although its liquid phase structure has not been determined, one can assume that extensive charge transfer still prevails, so that liquid strontium hydroxide can be considered as a molten salt. The temperature was fixed at 600 °C, much below the temperatures used up to now to obtain $Sr_4Mn_3O_{10}$.[16–19] This temperature falls also in the narrow stability range of molten $Sr(OH)_2$, which melts at 540 °C and decomposes at ~700 °C. The reaction time was screened in a second step, as reported later. A high concentration of manganese precursor ($KMnO_4$:$Sr(OH)_2$ = 1:65 mol.) was chosen to favour the nucleation step over growth, hence setting conditions suited to obtain relatively small particle size. After cooling down, the excess salt was eliminated by washing with diluted nitric acid until the supernatant reaches pH~5.

X-Ray Diffraction (XRD, **Figure S1**) shows that the $Sr_4Mn_3O_{10}$ phase is dispersed into $Sr(OH)_2$ in the crude final reaction medium. $Sr_4Mn_3O_{10}$ is obtained as a pure compound after washing according to XRD (**Figure S1**). Scanning electron microscopy (**Figure S3**) shows platelets with a large distribution of sizes, with basal faces ranging from ~100 nm to micrometers, and thickness dimensions up to ~100 nm. SEM and TEM showed only platelet morphologies with similar orientations analyzed by TEM. Indeed, TEM reveals crystalline mesoplatelets with a hexagonal basal face, an amorphous shell and corrugated lateral edges (**Figure 1A**). The SAED pattern of the crystalline area can be indexed along the [110] zone axis. Further characterization has been performed by atomic resolution high-angle annular dark-field imaging (HAADF) in the STEM mode of a microscope with aberration-correction in the probe. HAADF images are sensitive to the atomic number. Sr (Z=38) and Mn (Z=25) atomic columns are clearly differentiated (**Figure 1B**) and directly illustrate the $Sr_4Mn_3O_{10}$ structure, where Mn and Sr are 6- and 10-fold coordinated, respectively. The cationic distribution in the crystalline areas has been analyzed by monitoring simultaneously the Sr and Mn energy regions in electron energy loss spectroscopy (EELS) chemical mapping with atomic resolution (**Figure 1C-G**). Sr and Mn distributions are confirmed, with Mn octahedra trimers showing alternating orientations along the [001] direction. Noteworthy, (001) twinning occurs within the central part of the platelets (**Figures S2** and **1H**) and can be described as the result of a 180º rotation along the ***c*** axis (**Figure 1I**). Energy dispersive X-ray spectroscopy (EDS) shows that the crystalline areas exhibit the expected 4:3 Sr:Mn ratio **(Figure 1J**). Accordingly, the EELS spectrum of the Mn signal indicates only Mn (IV) in the crystalline part (**Figure 1K** and **1L**). Local chemical analysis has been performed to identify the amorphous component, mostly localized on the particle edges. EDS (**Figure 1J**) on these amorphous areas shows a decrease in the Sr:Mn ratio, pointing out a depletion of the Sr cations, while EELS (**Figure 1K**-**L**) indicates concomitant partial reduction of Mn^{4+} for charge compensation (**Table S1**). Note that partial substitution of O^{2-} by OH^- in the amorphous component would also result in reduction of Mn^{4+} and cannot be ruled out. The corresponding amorphous oxide can be precisely located by STEM-HAADF electron tomography coupled to contrast analysis. The 3D reconstructions (**Figure 1M** and **Movies S1** and **S2**) were obtained by using the Total Variation Minimization (TVM) method, which efficiently minimizes image distortions due to the missing wedge effect during the reconstruction (**Figure S4**). Electron tomography and scanning electron microscopy (**Figure S3**) show that the platelets are mostly flat, but also slightly oblong. In all cases, the edges are *ca.* 20 nm-thick. Hence, mesoscale platelets are actually nanostructured.

The corrugated, amorphous edges and the inner amorphous areas could be remnant of incomplete crystallization.[25] Because the temperature of synthesis is much lower than the typical melting point of such multicationic manganese oxides, any formation mechanism based on the solidification of a reactive melt can be precluded. Therefore,

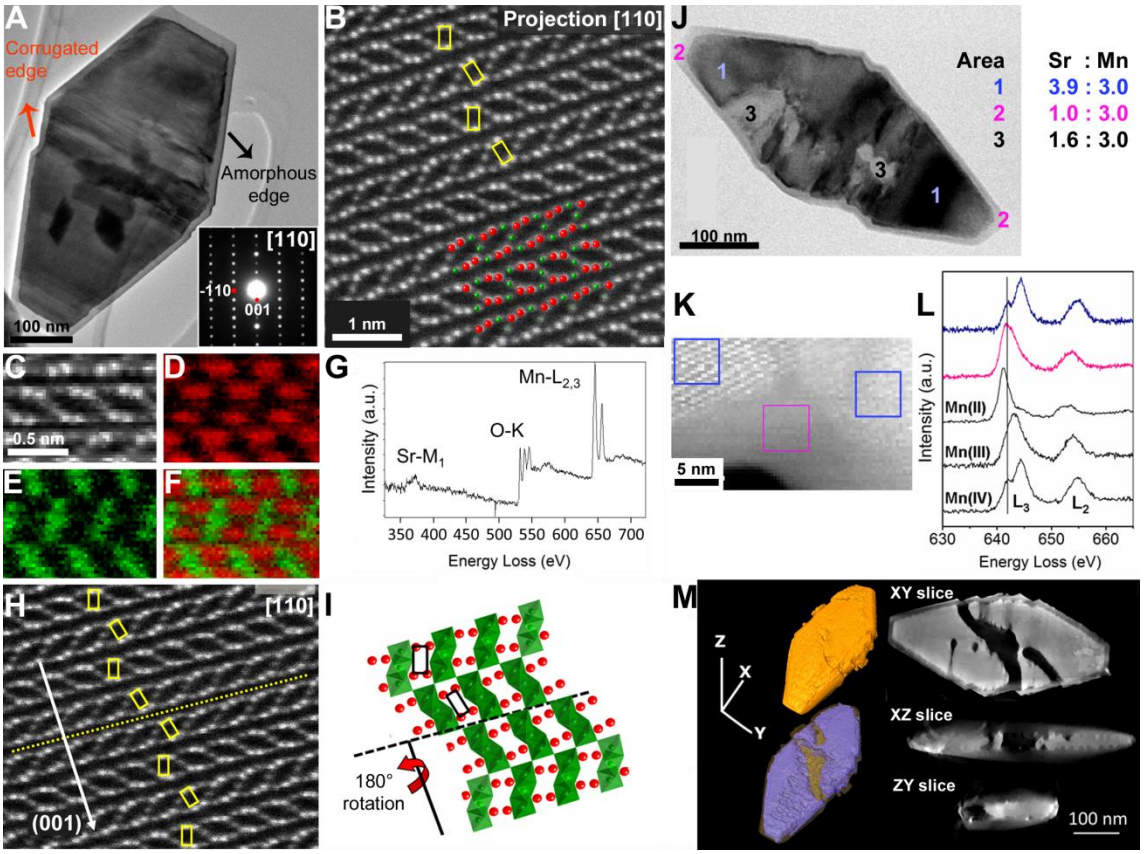

Figure 1. Structural and chemical information on $Sr_4Mn_3O_{10}$ mesoplatelets by TEM. (A) TEM image of a $Sr_4Mn_3O_{10}$ platelet. Inset: SAED pattern along the [110] zone axis. The black arrow shows the amorphous edge, and the red arrow a corrugated edge, observed on all particles studied. (B) Atomically-resolved Z-contrast HAADF image. The structural model is superimposed with Sr (red) and Mn (green) atom columns. Yellow squares symbolize face-sharing Mn octahedra trimers. (C) HAADF images acquired simultaneously with the EELS signal. (D) Sr-M_1, (E) Mn-$L_{2,3}$, (F) Sr and Mn chemical maps. (G) EELS spectrum obtained by integrating the signal from (C). (H) HAADF image showing a defect modelled in (I). (J) EDS analysis (mole ratios) of different crystalline (1) and amorphous (2,3) areas of a $Sr_4Mn_3O_{10}$ platelet. Chemical information on the edge of a $Sr_4Mn_3O_{10}$ particle: (K) HAADF signal acquired simultaneously with the Mn and Sr EELS signals. (L) High energy resolution Mn-$L_{2,3}$ EELS signals of the crystalline and amorphous regions (blue and purple squares in K, respectively). Mn(IV), Mn(III) and Mn(II) reference spectra are shown (black line). (M) HAADF electron tomography: topological reconstruction (yellow); orthoslices where dark areas show amorphous regions; reconstruction highlighting crystalline (blue) and amorphous zones (yellowish).

crystal growth occurs through precipitation in the molten salt following a chemical reaction. We then addressed the origin of the amorphous component by using state-of-the-art transmission electron microscopy. We have designed analytical STEM experiments to study the platelets within the reaction medium before washing with acidic water. The procedure relies on the specificities and advantages of HTIMS and high resolution analytical STEM, namely: (1) the high melting point that allows fast freezing and quenching of the reaction medium (temperature drops below the melting point (535 °C) in about 15 min); (2) the low vapour pressure and relatively high stability under the electron beam damage compared to organic solvents; and (3) the possibility to perform observations at low voltage (80 kV) with an aberration-corrected microscope with retained high resolution, even at low dose.

We investigated the early stages (1-2h) of crystallization of the native states (**Figure 2A-D**), thus providing a time series of the particles evolution. At each reaction time (1, 2 and 72 h), we took special care to ascertain reproducibility and to assess by STEM-HAADF that similar morphological and structural features are observed on different particles, whether their size, by analyzing ~30 particles. At 1 h, $Sr_4Mn_3O_{10}$ particles are already formed. EDX analysis (**Figure S5**A) shows that only Sr and Mn cations are present in the particles within the reaction media, while EELS (**Figure S5**B) indicates that the same particles contain only Mn^{4+} species. Therefore, no impurity could be detected and the particles are solely made of $Sr_4Mn_3O_{10}$. Furthermore, STEM-HAADF demonstrates that the platelets are fully crystalline without any evidence of amorphous areas (inset **Figure 2B**). Therefore, amorphization occurs during the purification step and must not be traced back to the solid formation events: Sr^{2+} is dissolved upon contact with acidic water (pH~5) during washing, thus corresponding to a leaching process. For lower pH values, the sample is completely amorphized. This washing procedure down to pH~5 appears as the best compromise to wash away the remaining hydroxide while avoiding the formation of large amounts of carbonates. Note that the potential role of oxidizing properties of nitrate anions on the amorphization process can be ruled out, as the mean oxidation state of Mn in the amorphous part is reduced.

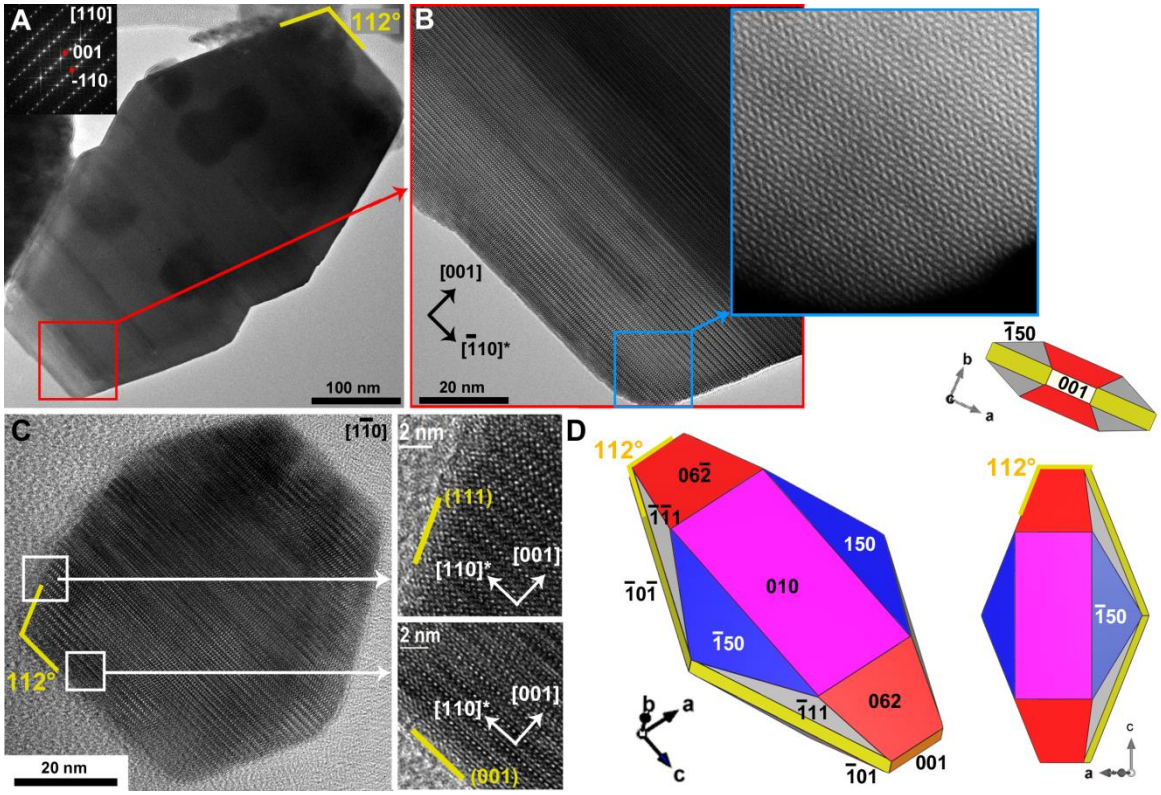

Figure 2. Single crystal features of $Sr_4Mn_3O_{10}$ mesoplatelets, obtained after (A-B) 2 h and (C) 1 h, observed directly in the salt medium. (A, B, C) TEM micrographs and SAED pattern (A inset) showing the absence of amorphous areas. HAADF (B inset) and HRTEM enlargements (C insets) highlight the fully crystalline state prior to washing. (D) Corresponding 3D model, [1-10] (bottom) and [001] (top) projections of a platelet.

Particles in the native state exhibit two kinds of line defects: {001} twinning and staking faults parallel to {111} facets (**Figure 3A-C**). After a short heat treatment (1 h, **Figure 3B-C**), some particles exhibit an intermediate stage with corrugated edges and inner contrast variations highlighting a high density of defects. High resolution micrographs and corresponding Fourier transforms demonstrate the nearly perfect alignment of lattice fringes along the whole platelets across the coalescence areas. Both the crystalline and amorphous components of water-washed particles identified by HAADF electron tomography (**Figure 3D-G**) also shows line defects parallel to {001} and {111} facets. Amorphization appears at reactive areas of the pristine particles: edges that are thinner than the platelet core, and areas showing high density of {001} and {111} defects.

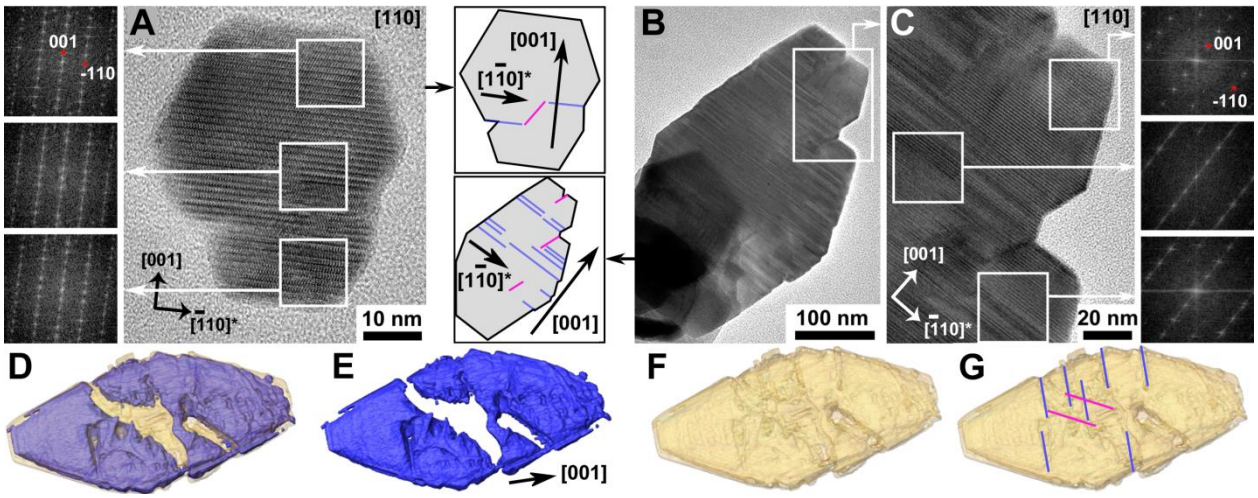

Figure 3. Location of crystal defects and its impact on the amorphous component. Platelets (A-C) observed directly from the salt medium after 1 h of heating. (A-C) TEM micrographs and corresponding Fourier transforms showing the alignment of lattice fringes from different areas; schemes highlight the {001} (blue) and {111} (purple) faults. (D-F)

STEM-HAADF tomographic reconstruction of a platelet after 72 h of dwell time followed by washing, showing the crystalline (blue) and amorphous (yellowish) components. (G) {001} (blue) and {111} (purple) faults highlighted from the topology of the amorphous component (F) and the depressions in the crystalline component (E).

To assess the role that surface Coulombic interactions may play on the observed platelet morphology, (001), (-111) and the composite {010}/{150}/{062} basal faces were designed (**Figures S8, S9**) to expose the highest amount of strontium coordination polyhedra (5.8, 6.5 and 5.8 Sr·nm^{-2}, respectively). The composite basal faces have been approximated to {010} terraces with {100}, {101} and {001} steps (**Figure S8**). These Sr-saturated facets account for the excess of molten strontium hydroxide as growth medium and should be considered as rough approximations of the actual surface states. Surface charges were calculated by considering the bond valences of surface ions (**SI, figure S9**). The stepwise {010} basal faces exhibit the lowest charge. This difference in surface charge provides a possible explanation for the formation of highly anisotropic mesostructures like mesoplatelets. Indeed, the extent of highly charged facets of oxides in polar liquids is usually minimized, because high charge density destabilizes surfaces by Coulombic repulsion between the charged oxygen-bearing groups. This is especially recognized for first row transition metal (oxyhydr)oxides,[26–32] for which highly charged surfaces bear the highest surface energy and are then exposed to the lowest extent.

Finally, manganese oxides are promising cheap and precious metal-free catalysts for the oxygen reduction reaction (ORR) in water-based devices.[33–36] $Sr_4Mn_3O_{10}$ platelets provide a unique opportunity to assess the activity of this phase whose properties have never been investigated. The electrocatalytic activity was studied by standard methods using a composite carbon black/Nafion/oxide particles thin film rotating electrode in a O_2-saturated 0.1 mol L^{-1} KOH electrolyte (**Figure 4A**). For $Sr_4Mn_3O_{10}$, the ORR onset occurs at ~0.80 V *versus* the reversible hydrogen electrode (RHE) and an oxygen-transport-limited current appears below 0.5 V/RHE (**Figure 4B**). The Koutecky-Levich analysis of the mass-transport-limited region (0.4 V/RHE) (**Figure 4B** inset) indicates a 3.7 electron mechanism, in agreement with a 4 electron-reduction reaction of oxygen to water (**Figure S10**). Oxide surface-normalized current densities (**Figure 4C**) are stable over the first 5 cycles (**Figure S11**). TEM does not show any morphological and structural changes, as the amorphous edges are not extending over several hours (not shown). Overall, $Sr_4Mn_3O_{10}$ platelets bearing an amorphous manganese oxide shell with mixed $Mn^{3+/4+}$ redox exhibit ORR activity, as previously reported for mixed valence manganese (III)/(IV) oxides.[36] Hence, the amorphous surface layer in contact with the electrolyte drives the ORR electrocatalytic properties.

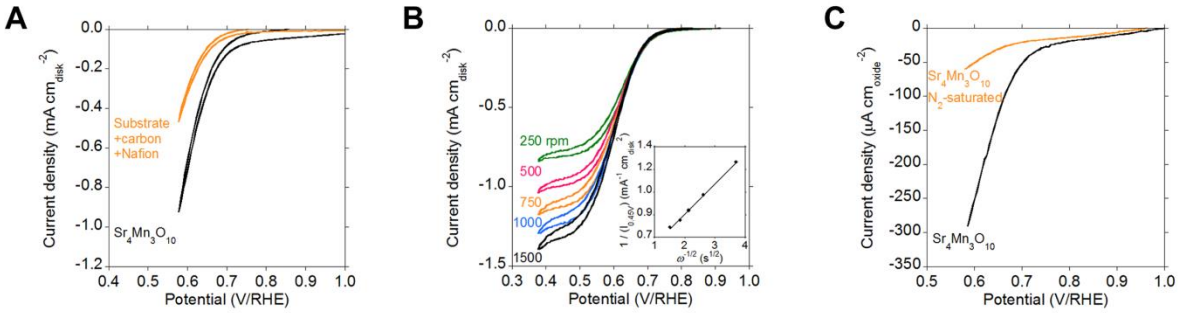

Figure 4. Oxygen reduction reaction electrocatalysis. (A) Electrocatalytic ORR activity of platelets obtained after 72 h, investigated by cyclic voltammetry at 10 mV s^{-1} scan rate and 1600 rpm. The 5th cycle is shown and compared to an electrode without catalyst. (B) ORR of a $Sr_4Mn_3O_{10}$ electrode at different rotation rates, with the corresponding Koutecky–Levich analysis of the limiting currents at 0.45 V (inset). (C) Oxide surface-normalized ORR current densities corrected from the capacitive current and the contribution of the carbon black/Nafion additive.

Conclusions

To conclude, we have shown that by using a reactive molten salt, a multicationic manganese oxide can be synthesized as nanostructured mesoplatelets. This study provides the first occurrence of this compound at the mesoscale. Hence, molten salts are efficient media to grow crystalline oxide nano/meso-structures that are unreported in terms of faceting and crystal habits, but they also provide new structures and compositions at the nano/meso-scale. A strongly anisotropic morphology has been obtained without addition of surface complexing agents. Although the exact reaction mechanism deserves in-depth investigation out of the scope of this article, the peculiar platelet morphology can be explained by the difference in surface charge and then surface energy of the different facets, when they are in contact with the molten ionic medium. With this work we provide clear evidence that molten salts are relevant media to target new oxide-based mesoscaled materials without any organic surface ligands, with certainly large future impact in the fields of catalysis and energy conversion.

Conflicts of interest

There are no conflicts of interest to declare.

Acknowledgements

Financial support through Research Project CSD2009-00013 (Spain), CNRS, UPMC and Collège de France is acknowledged. J.C.H.-G. acknowledges support from the Ramón y Cajal

Fellowships Program of MINECO (RYC-2012-10004). M.L.-H. acknowledges support from the Juan de la Cierva Fellowships Program of MINECO (IJCI-2014-19367). HAADF-STEM images were acquired at SC-ICYT UCA with financial support from MINECO/FEDER Project Ref: MAT2013-40823-R.

Notes and references

1 X. Liu, N. Fechler and M. Antonietti, *Chem. Soc. Rev.*, 2013, **42**, 8237–8265.
2 M. J. Bojdys, J.-O. Müller, M. Antonietti and A. Thomas, *Chem. Eur. J.*, 2008, **14**, 8177–8182.
3 H. Le Thi N'Goc, L. D. N. Mouafo, C. Etrillard, A. Torres-Pardo, J.-F. Dayen, S. Rano, G. Rousse, C. Laberty-Robert, J. G. Calbet, M. Drillon, C. Sanchez, B. Doudin and D. Portehault, *Adv. Mater.*, 2017, **29**, 1604745.
4 J. S. Kanady, P. Leidinger, A. Haas, S. Titlbach, S. Schunk, K. Schierle-Arndt, E. J. Crumlin, C. H. Wu and A. P. Alivisatos, *J. Am. Chem. Soc.*, 2017, **139**, 5672–5675.
5 T. Xu, X. Zhou, Z. Jiang, Q. Kuang, Z. Xie and L. Zheng, *Cryst. Growth Des.*, 2009, **9**, 192–196.
6 C. Xu, X. Zhao, S. Liu and G. Wang, *Solid State Commun.*, 2003, **125**, 301–304.
7 P. Zhang, J. Liu, H. Du, S. Li and R. Xu, *Chem. Commun.*, 2010, **46**, 3988.
8 Y. Dong, K. He, L. Yin and A. Zhang, *Nanotechnology*, 2007, **18**, 435602.
9 Y. Chen, B. Chi, Q. Liu, D. C. Mahon and Y. Chen, *Chem. Commun. (Camb).*, 2006, 2780–2782.
10 D. Portehault, S. Devi, P. Beaunier, C. Gervais, C. Giordano, C. Sanchez and M. Antonietti, *Angew. Chem. Int. Ed.*, 2011, **50**, 3262–3265.
11 S. Carenco, D. Portehault, C. Boissière, N. Mézailles and C. Sanchez, *Chem. Rev.*, 2013, **113**, 7981–8065.
12 G. Gouget, P. Beaunier, D. Portehault and C. Sanchez, *Faraday Discuss.*, 2016, **191**, 511–525.
13 J. Ma, Y. Gu, L. Shi, L. Chen, Z. Yang and Y. Qian, *J. Alloys Compd.*, 2004, **370**, 281–284.
14 W. Lei, D. Portehault, R. Dimova and M. Antonietti, *J. Am. Chem. Soc.*, 2011, **133**, 7121–7127.
15 D. Portehault, S. Cassaignon, E. Baudrin and J.-P. Jolivet, *J. Mater. Chem.*, 2009, **19**, 2407.
16 J. Fábry, J. Hybler, Z. Jirák, K. Jurek, K. Malý, M. Nevřiva and V. Petříček, *J. Solid State Chem.*, 1988, **73**, 520–523.
17 N. Floros, M. Hervieu, G. van Tendeloo, C. Michel, A. Maignan and B. Raveau, *Solid State Sci.*, 1998, **2**, 1–9.
18 N. Floros, M. Hervieu, G. Van Tendeloo, C. Michel, a. Maignan and B. Raveau, *Solid State Sci.*, 2000, **2**, 1–9.
19 H. Yang, Y. K. Tang, J. L. Jiang, W. J. Feng, Z. Q. Wei, L. D. Yao, W. Zhang, Q. A. Li, F. Y. Li, C. Q. Jin and R. C. Yu, *J. Mater. Sci.*, 2007, **42**, 9559–9564.
20 K. Kimoto, T. Asaka, T. Nagai, M. Saito, Y. Matsui and K. Ishizuka, *Nature*, 2007, **450**, 702–4.
21 C. Kisielowski, B. Freitag, M. Bischoff, H. van Lin, S. Lazar, G. Knippels, P. Tiemeijer, M. van der Stam, S. von Harrach, M. Stekelenburg, M. Haider, S. Uhlemann, H. Müller, P. Hartel, B. Kabius, D. Miller, I. Petrov, E. A. Olson, T. Donchev, E. A. Kenik, A. R. Lupini, J. Bentley, S. J. Pennycook, I. M. Anderson, A. M. Minor, A. K. Schmid, T. Duden, V. Radmilovic, Q. M. Ramasse, M. Watanabe, R. Erni, E. A. Stach, P. Denes and U. Dahmen, *Microsc. Microanal.*, 2008, **14**, 469–477.
22 D. a Muller, *Nat. Mater.*, 2009, **8**, 263–70.
23 M. Hernando, L. Miranda, A. Varela, K. Boulahya, S. Lazar, D. C. Sinclair, J. M. González-Calbet and M. Parras, *Chem. Mater.*, 2013, **25**, 548–554.
24 M. Mérawa, B. Civalleri, P. Ugliengo, Y. Noël and A. Lichanot, *J. Chem. Phys.*, 2003, **119**, 1045–1052.
25 V. K. La Mer and H. Dinegar, *J. Am. Chem. Soc.*, 1950, **72**, 4847–4854.
26 D. Portehault, S. Cassaignon, E. Baudrin and J.-P. Jolivet, *Cryst. Growth Des.*, 2009, **9**, 2562–2565.
27 D. Portehault, S. Cassaignon, E. Baudrin and J.-P. Jolivet, *J. Mater. Chem.*, 2009, **19**, 7947.
28 I. M. Description and P. Nutrition, *Interface*.
29 J. P. Jolivet, C. Froidefond, A. Pottier, C. Chanéac, S. Cassaignon, E. Tronc and P. Euzen, *J. Mater. Chem.*, 2004, **14**, 3281–3288.
30 D. Peng, S. Beysen, Q. Li, Y. Sun and L. Yang, *Particuology*, 2010, **8**, 386–389.
31 T. Saison, N. Chemin, C. Chanéac, O. Durupthy, V. Ruaux, L. Mariey, F. Maugé, P. Beaunier and J.-P. Jolivet, *J. Phys. Chem. C*, 2011, **115**, 5657–5666.
32 D. Portehault, S. Cassaignon, E. Baudrin and J.-P. Jolivet, *Cryst. Growth Des.*, 2010, **10**, 2168–2173.
33 J.-J. Xu, D. Xu, Z.-L. Wang, H.-G. Wang, L.-L. Zhang and X.-B. Zhang, *Angew. Chemie Int. Ed.*, 2013, **52**, 3887–3890.
34 J. Suntivich, H. a Gasteiger, N. Yabuuchi, H. Nakanishi, J. B. Goodenough and Y. Shao-Horn, *Nat. Chem.*, 2011, **3**, 546–550.
35 M. Risch, K. A. Stoerzinger, S. Maruyama, W. T. Hong, I. Takeuchi and Y. Shao-Horn, *J. Am. Chem. Soc.*, 2014, **136**, 5229–5232.
36 K. A. Stoerzinger, M. Risch, B. Han and Y. Shao-Horn, *ACS Catal.*, 2015, **5**, 6021–6031.

Supplementary Information

Multicationic $Sr_4Mn_3O_{10}$ mesostructures: molten salt synthesis, analytical electron microscopy study and reactivity

Irma N. González-Jiménez,[a] Almudena Torres-Pardo,[a,b] Simon Rano,[c] Christel Laberty-Robert,[c] Juan Carlos Hernández-Garrido,[d,e] Miguel López-Haro,[d,e] José J. Calvino,[d,e] Áurea Varela,[a] Clément Sanchez,[c] Marina Parras,[a,*] José M. González-Calbet,[a,f] David Portehault[c,*]

[g.] *Departamento de Química Inorgánica, Facultad de CC. Químicas, Universidad Complutense de Madrid, 28040 Madrid, Spain,E-mail: mparras@quim.ucm.es*

[h.] *CEI Campus Moncloa, UCM-UPM, Madrid, Spain.*

[i.] *Sorbonne Université, CNRS, Collège de France, Laboratoire Chimie de la Matière Condensée de Paris, LCMCP, 4 Place Jussieu, F-75005 Paris, France. E-mail: david.portehault@sorbonne-universite.fr*

[j.] *Departamento de Ciencia de los Materiales e Ingeniería Metalúrgica y Química Inorgánica, Facultad de Ciencias, Universidad de Cádiz, Campus Río San Pedro S/N, Puerto Real 11510 (Cádiz), Spain.*

[k.] *Instituto Universitario de Investigación de Microscopía Electrónica y Materiales (IMEYMAT). Facultad de Ciencias. Universidad de Cádiz. Campus Río San pedro S/N, Puerto Real 11510 (Cádiz), Spain.*

[l.] *Centro Nacional de Microscopía Electrónica, Universidad Complutense, 28040 Madrid, Spain.*

MATERIALS AND METHODS

FIGURES

TABLES

MOVIE S1. STEM-HAADF tomography of platelet, showing the crystalline component (blue) and the amorphous one (gold).

MOVIE S2. STEM-HAADF tomography of platelet, showing separately the crystalline component (blue) and the amorphous one (gold).

MATERIALS AND METHODS

Materials. $Sr(OH)_2 \cdot 8H_2O$, $KMnO_4$ and HNO_3 were purchased from Sigma-Aldrich. All chemicals were used as received. Water was purified through a Milli-Q Millipore system.

Synthesis. $Sr(OH)_2 \cdot 8H_2O$ and $KMnO_4$ (99+ %) were mixed in a molar ratio 65:1 (0.19 mmol of $KMnO_4$) and ground finely with a Retsch MM400 ball mill (airtight vials of 50 mL, one ball of 62.3 g and a diameter of 23 mm) for 2 min at 60 Hz. The resulting powder was transferred in a glassy carbon crucible, dehydrated in a vacuum oven at 40 ºC overnight and then heated at 600 ºC under Ar flow and Schlenk line conditions. Water evolved at *ca.* 300 °C. After being cooled down to room temperature, the obtained powders were dissolved in argon-saturated water to which HNO_3 (69%) was added dropwise until pH~5 was reached. The final powder was recovered after centrifugation, washed with Ar-saturated water 4 times and dried at 40 ºC in a vacuum oven. The final yield is *ca.* 80 %.

Scanning electron microscopy (SEM). SEM micrographs were acquired in a JEOL JSM 6335-FEG scanning microscope operating at an acceleration voltage of 5 kV.

Selected Area Electron Diffraction (SAED) and High Resolution Transmission Electron Microscopy (HRTEM) were performed on a JEOL 300FEG electron microscope. Chemical composition of the mesocrystals was determined by energy-dispersive **X-ray spectroscopy (EDS)** in both JEOL JSM6335-FEG and JEOL 300FEG electron microscopes. Mn-Kα_1 and Sr-K α_1 spectral lines were used for determination of Sr:Mn molar ratio over 30 particles. Standard deviations for the Sr:Mn ratios indicated in Figure 1J are 1.4 in areas 1 and 2; 3.9 in area 3. Atomic resolution images were acquired on a JEOL JEMARM200cF electron microscope (Cold Emission Gun) with a spherical aberration corrector in the probe (current emission density ~$1.4 \cdot 10^{-9}$ Å and probe size ~0.08 nm), coupled with a GIF-QuantumER spectrometer. We operated at 200 kV for pure $Sr_4Mn_3O_{10}$ samples and at 80 kV for those samples before washing. Solid semi-angles between 68–280 mrad were used for acquisition of HAADF images (38 s per frame). Atomically-resolved **Electron Energy Loss Spectroscopy (EELS)** maps were acquired with a spatial resolution ~0.1 nm, over a total acquisition time ~2 min (current emission density of ~1.2×10^8 A and a probe size of ~0.12 nm). Principal component analysis (PCA) with 8 components was performed on EELS data set to de-noise the spectra by using the Hyperspy data analysis toolbox. The Mn oxidation state was analyzed from the Energy-Loss Near-Edge fine Structure (ELNES) of Mn-$L_{2,3}$ signals. High energy resolution punctual EELS spectra were acquired over ~0.5 nm area with energy dispersion of 0.1 eV and 2 mm spectrometer aperture. The total acquisition time was optimized to 10 s in order to prevent beam-damage of the sample. Dual-EELS function of the GIF-QuantumERTM spectrometer, allowing the simultaneous acquisition of two different energy ranges, was used to record simultaneously the zero-Loss peak (10^{-4} s exposition time, 10 frames) and the Mn-$L_{2,3}$ core-region (1 s exposition time, 10 frames) in order to minimize the uncertainty on the energy shift of the Mn-$L_{2,3}$ edges. With the aim of analyzing the EELS experimental data obtained from the $Sr_4Mn_3O_{10}$ sample, EELS spectra were recorded from three valence standard samples: $Ca_2Mn_3O_8$ (Mn IV), $LaMnO_3$ (Mn III) and $Ca_2Mn_3O_5$ (Mn II).

Electron tomography experiments based on high-angle annular dark-field (HAADF) imaging in the scanning transmission electron microscopy (STEM) mode were performed on a JEOL 2010F electron microscope tilting the sample ±76° about a single axis using a Fischione 2030 ultra-narrow gap tomography holder. Tomography experiments based on high-angle annular dark-field (HAADF) imaging in the scanning transmission electron microscopy (STEM) mode were performed on a JEOL 2010F electron microscope operating at 200kV .The sample was tilted ±76° about a single axis using a Fischione 2030 ultranarrow gap tomography holder. Tilt series were aligned using Inspect3D software and reconstructed by Compressed Sensing technique. In particular, Total Variation Minimization (TVM) was carried out using the TVAL3 solver (C. Li, Rice University, 2010) with projections and back-projections operators from the ASTRA Toolbox (W. van Aarle, W. J. Palenstijn, J. De Beenhouwer, T. Altantzis, S.

Bals, K. J. Batenburg, and J. Sijbers, *Ultramicroscopy*, 2015, **157**, 35–47.), using GPU implementation for gain in rapidity. The reconstructed volume was thereafter segmented automatically using Multi-Otsu threshold implemented in Matlab and Amira software was used to visualize the 3D volume.

X-ray diffraction (XRD). XRD patterns were obtained by using a Panalytical X'Pert Pro Alpha1 instrument, equipped with a primary fast X'Celerator detector operating at 45 kV and 40 mA, and fitted with a primary curved Ge 111 monochromator in order to get the Cu $K_{\alpha 1}$ radiation (λ = 1.5406 Å). Data were collected at 2θ between 5º and 70º, with a step size of 0.04º and a collection time of 1 sec/step at room temperature.

Electrochemical characterization. The rotating disk electrode (RDE) was prepared by coating a glassy carbon (GC) disk electrode (0.07 cm², Radiometer Analytical) previously polished with diamond paste (1 µm, BAS inc.) followed by alumina paste (0.05 µm, BAS inc.) to reach mirror grade. A conductive ink containing the catalyst was then coated over the substrate:

Ink preparation. This ink was prepared from three components: the catalyst powder, Acetylene Black (AB, Alfa Aesar) (99.9+ %, 75 $m^2 \cdot g^{-1}$) and Nafion-117 solution (5% in aliphatic alcohol, Sigma-Aldrich). The Nafion-117 solution was previously ion-exchanged with Na^+ by slowly adding 1 mL of NaOH 0.1 M solution to 2 mL of Nafion alcoholic solution under stirring, followed by stirring during 5 minutes. The acetylene black powder was hydrophilized by dispersing 500 mg of AB in 50 mL of HNO_3 20 % at 80 °C overnight under stirring, followed by centrifugation and washing with water and vacuum drying. The ink was prepared by dispersing 10 mg of catalyst powder in 10 mL of ethanol (99%), along with 10 mg of treated AB. The mixture was sonicated in a water bath for 2 hours. Then, the dispersion was cooled to room temperature and dispersed with a sonic horn for 5 minutes. 347 µL of ion-exchanged Nafion solution was then added immediately. The ink was sonicated for 5 minutes and remained stable and aggregate free for at least 1 week.

Electrode preparation. After few minutes of horn sonicating in cool conditions, 1 µL of the ink was deposited on the GC substrate. The film was dried in a closed beaker for 20 min. Then, the electrode was transferred in an oven where it was dried for 1 hour at 60 °C. The prepared electrode consisted in a black film coated on the GC RDE with an oxide content of 15 $\mu g \cdot cm^{-2}_{disk}$.

Electrochemical characterization. The freshly prepared electrode was characterized with a three-electrode setup, with the RDE as the working electrode, a Pt wire as counter electrode and a Ag/AgCl electrode as reference. The setup was connected to a Solartron Analytical device potentiostat. Prior to electrochemical experiments, the working electrode was hydrated with the 0.1 M KOH electrolyte over 20 min. All cyclic voltammetry experiments were performed in either O_2 or N_2 (Air Liquid) saturated electrolyte at a scan rate of 10 $mV \cdot s^{-1}$. Capacity-corrected currents were obtained by averaging the potential over each reduction-oxidation cycle. To normalize the current versus the oxide surface, the specific surface area was evaluated at 6 $m^2 \cdot g^{-1}$ for $Sr_4Mn_3O_{10}$ according to geometrical calculations. Each experiment was repeated at least 3 times.

MUSIC^2 model. The charge of the different facets was evaluated by adapting the MUSIC^2 model (T. Hiemstra, W. Riemsdijk, G. H. Bolt, Multisite Proton Adsorption Modeling at the Solid/Solution Interface of (hydr)oxides: a new approach. I. Model Description and Evaluation of Intrinsic Reaction Constants. *J. Colloid Interf. Sci.* **133**, 91 (1989); T. Hiemstra, P. Venema, W. Riemsdijk, Intrinsic Proton Affinity of Reactive Surface Groups of Metal (Hydr)oxides: the Bond Valence Principle. *J. Colloid Interf. Sci.* **184**, 680–692 (1996)). The model considers effective valences *s* (L. Pauling, The Principles determining the Structure of Complex Ionic Crystals. *J. Am. Chem. Soc.* **51**, 1010 (1929)) of metal-oxygen bonds s_{Me} from Brown's and Altermatt's approach (I. D. Brown, I. D. Altermatt, Bond-Valence Parameters obtained from a Systematic Analysis of the Inorganic Crystal Structure Database. *Acta Cryst.* **B41**, 244 (1985)):

$$s = \exp[(r_0 - r)/B]$$

where r is the bond length, r_0 and B are empirical parameters (I. D. Brown, I. D. Altermatt, Bond-Valence Parameters obtained from a Systematic Analysis of the Inorganic Crystal Structure Database. *Acta Cryst.* **B41**, 244 (1985)):

$r_0(Mn^{4+}\text{-}O) = 1.753$ Å; $r_0(Sr^{2+}\text{-}O) = 2.118$ Å; $B(Mn^{4+}\text{-}O) = 0.370$; $B(Sr^{2+}\text{-}O) = 0.370$.

In bulk crystals, the electroneutrality principle implies that the sum of effective bond valences for a given atom and its valence (oxidation state) V is equal to 0. However, surface atoms experience frustrated coordination, so that the residual charge q on the surface group is equal to the sum of its effective bond valences (s) and its oxidation state:

$$q = V + \sum s$$

For hydroxo and oxo groups, the following equations apply:

$$q_{OH} = -1 + \sum s_{Me}$$

$$q_O = -2 + \sum s_{Me}$$

Where s_{Me} is the effective bond valence of each metal-oxygen bond. The model can also take into account charge transfer due to hydrogen bonds and yields similar expressions in our case (I. D. Brown, Geometry of O-H...O Hydrogen bonds. *Acta Cryst.* **A32**, 786 (1976)).

The MUSIC[2] model (T. Hiemstra, W. Riemsdijk, G. H. Bolt, Multisite Proton Adsorption Modeling at the Solid/Solution Interface of (hydr)oxides: a new approach. I. Model Description and Evaluation of Intrinsic Reaction Constants. *J. Colloid Interf. Sci.* **133**, 91 (1989); T. Hiemstra, P. Venema, W. Riemsdijk, Intrinsic Proton Affinity of Reactive Surface Groups of Metal (Hydr)oxides: the Bond Valence Principle. *J. Colloid Interf. Sci.* **184**, 680–692 (1996)) uses the residual charge q to evaluate the acidity constant of each aquo, hydroxo and oxo surface groups. In our case, the following equations apply:

$$pK_A^{HO/O} = -19.8\ (q_O)$$

$$pK_A^{H2O/OH} = -19.8\ (q_{OH})$$

By using this acidity constant, the surface density of each oxo and hydroxo group can be evaluated as a function of pH. By combining these speciation curves with the corresponding residual charges q, a theoretical evolution of the surface charge as a function of the pH can be retrieved. In highly basic media, aquo groups are unlikely to exist, so that we focused only on hydroxo, oxo groups and the first acidity constant $pK_A^{HO/O}$. Importantly, the model does not take into account electrostatic repulsions between neighbouring charged surface groups. Accordingly, experimental surface charge densities are lower than those retrieved from the model. Therefore, calculated values of charge densities should not be used for quantitative purpose but only for comparison between the different facets.

Although the model was originally developed to account for oxide surfaces in contact with water, it may still be applied in molten hydroxide, bearing in mind that the actual "pH" value should be adjusted to yield the highest amount of μ_1 (oxygen bonded to one metal cation), and μ_2 (oxygen bridging 2 metal cations) hydroxo groups bonded to surface Sr^{2+} ions. On the contrary, μ_4 hydroxo groups are unlikely because electron density on oxygen ions is strongly dragged by neighbouring metal cations. These considerations lead to focus studies on the highlighted "pH" area in **Figure S10**, between "pH" 20 and 30.

FIGURES

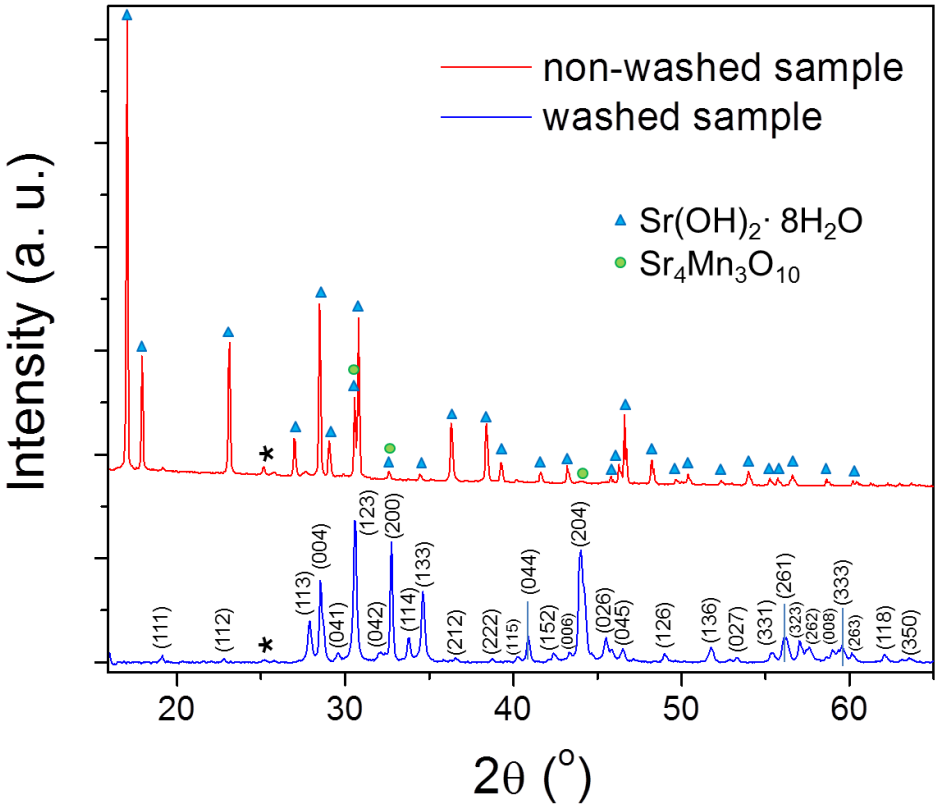

Figure S1. XRD patterns of the crude reaction medium at room temperature and exposed to air (red) and a sample washed with HNO_3 (blue). $Sr_4Mn_3O_{10}$ is always obtained after washing, as seen in (blue pattern) where all the maxima can be assigned to an orthorhombic cell of the *Cmca* space group. Experimental cell parameters a = 0.547 nm, b = 1.238 nm, c = 1.251 nm are in good agreement with the reference ones a = 0.544 nm, b = 1.243 nm, c = 1.250 nm (J. Fábry et al., Preparation and the crystal structure of a new manganate, $Sr_4Mn_3O_{10}$. *J. Solid State Chem.* **73**, 520–523, 1988 and N. Floros, M. Hervieu, G. van Tendeloo, C. Michel, A. Maignan, and B. Raveau, The layered manganate $Sr_{4-x}Ba_xMn_3O_{10}$: synthesis, structural and magnetic properties. *Solid State Sci.*, 1998, **2**, 1–9). Prior to washing (red pattern), it is possible to distinguish some of the $Sr_4Mn_3O_{10}$ maxima (marked with green circles) concealed by the $Sr(OH)_2$ peaks. $SrCO_3$ contamination is also detected (marked with an asterisk).

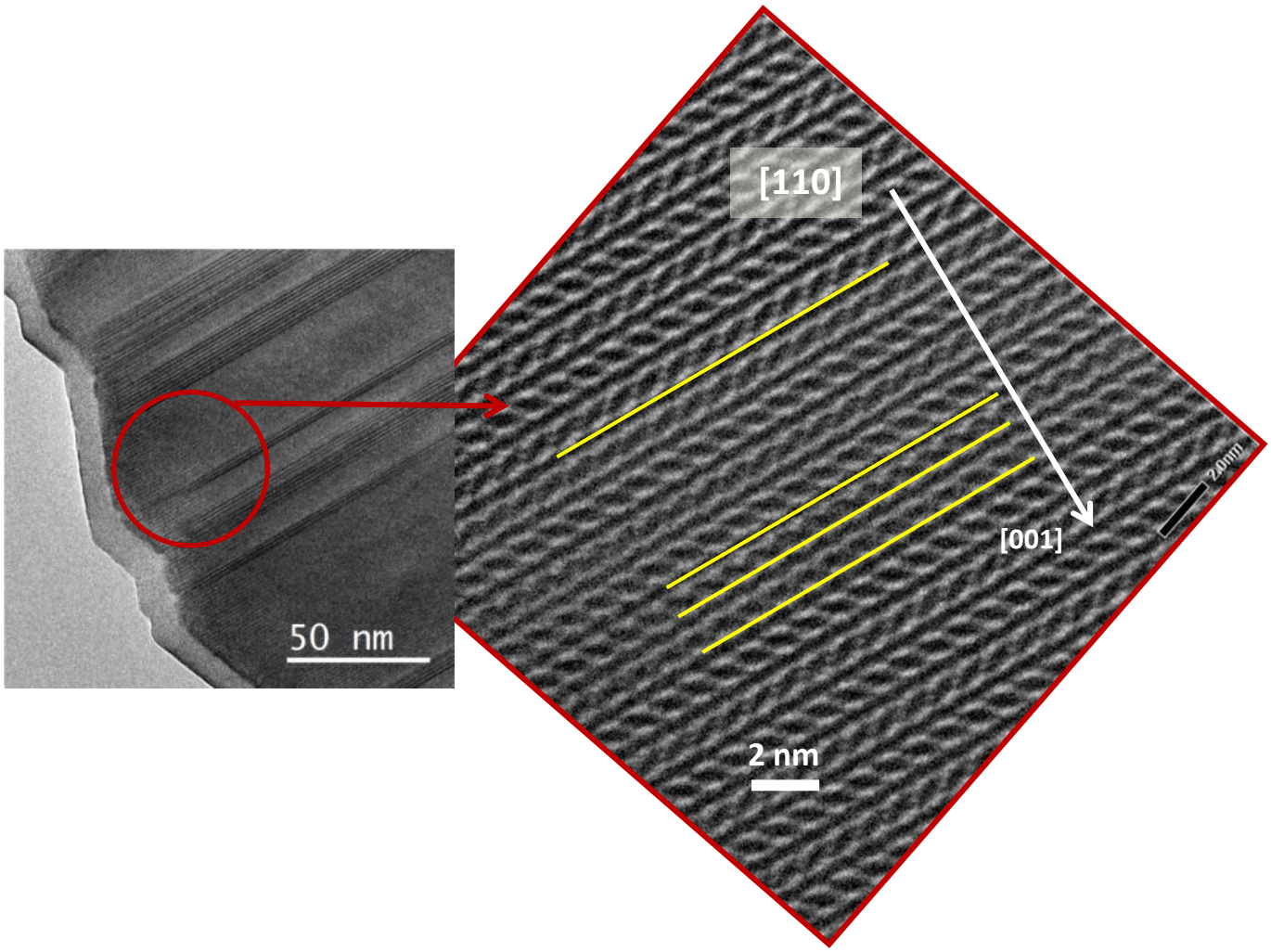

Figure S2. Low magnification TEM micrograph of a $Sr_4Mn_3O_{10}$ platelet showing twinning along (001) planes. A detailed atomic resolution image of a twin plane is shown in the enlargement.

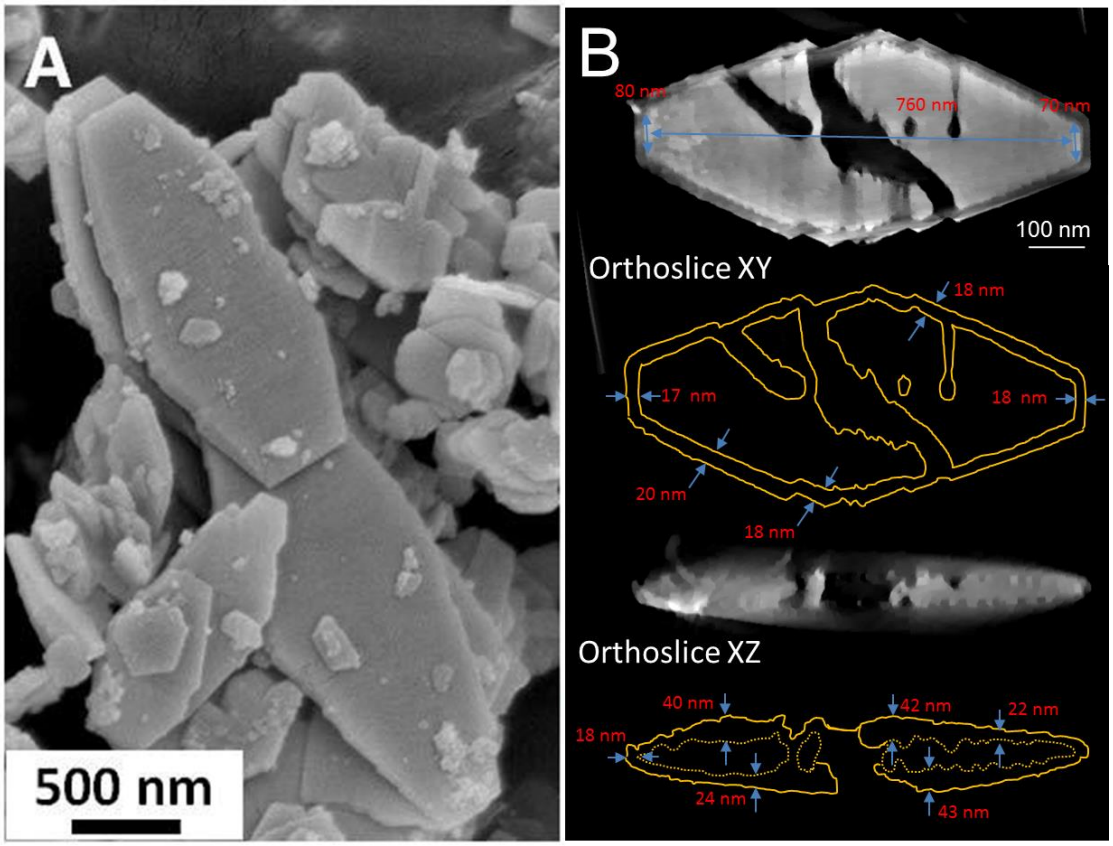

Figure S3. Topology and nanometrology of $Sr_4Mn_3O_{10}$ platelets. (A) SEM micrograph. (B) STEM-HAADF tomography. XY and XZ orthoslices from the 3D reconstruction of a $Sr_4Mn_3O_{10}$ particle and a model of its texture with distances and measurements of the thickness of the amorphous shell. 3D representations (**Figure 1M** and **Movie S1**) and SEM (**A**) show that the platelets are not flat but slightly oblong and get thinner at the edges, with thicknesses of 100 nm at the center and 20 nm at the edge. The width of the amorphous shell is ~20 nm.

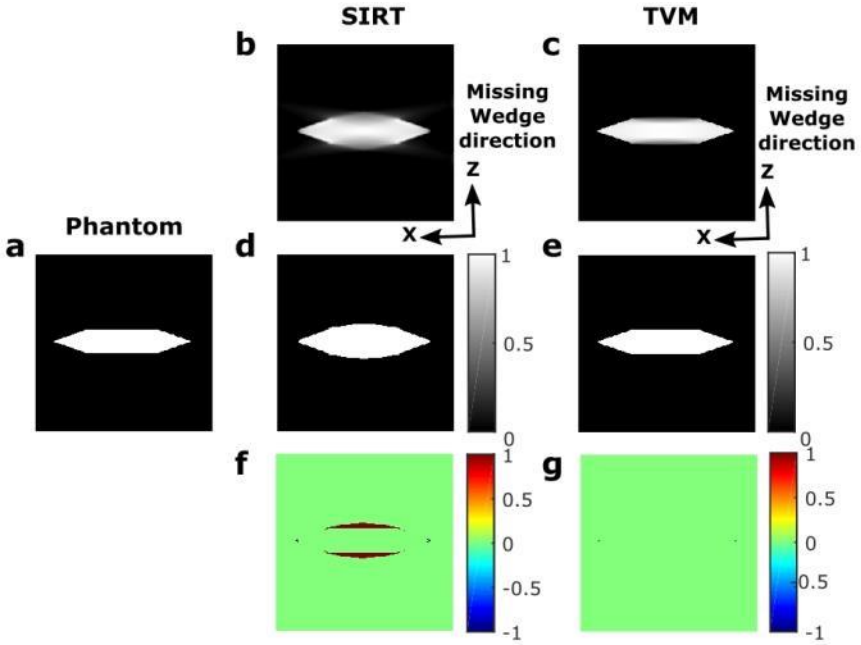

Figure S4. Transmission electron tomography: simulation of the volume reconstruction process. To test the fidelity of the tomographic reconstruction, a simple model was built (a) and re-projected from -76° to +76 ° every 2°. The model was reconstructed by two methods: (b) the well-known simultaneous iterative reconstruction technique (SIRT) using 100 iterations and (c) the Total Variation Minimization (TVM) algorithm using TVAL3 solver. Segmentation of the reconstructed model by SIRT (d) and TVM (e) was carried out automatically using the Otsu thresholding. To map the residual error, the difference between the original object and the segmented reconstruction was calculated (f-g). The limitation of the maximum tilt angle during the electron tomography acquisition results in an artificial elongation along the z axis after the volume reconstruction, called the missing wedge artifact. However, the TVM algorithm is able to reduce the artifact, thus providing a morphology closer to the original object. This is TVM reconstruction that is used in the whole manuscript.

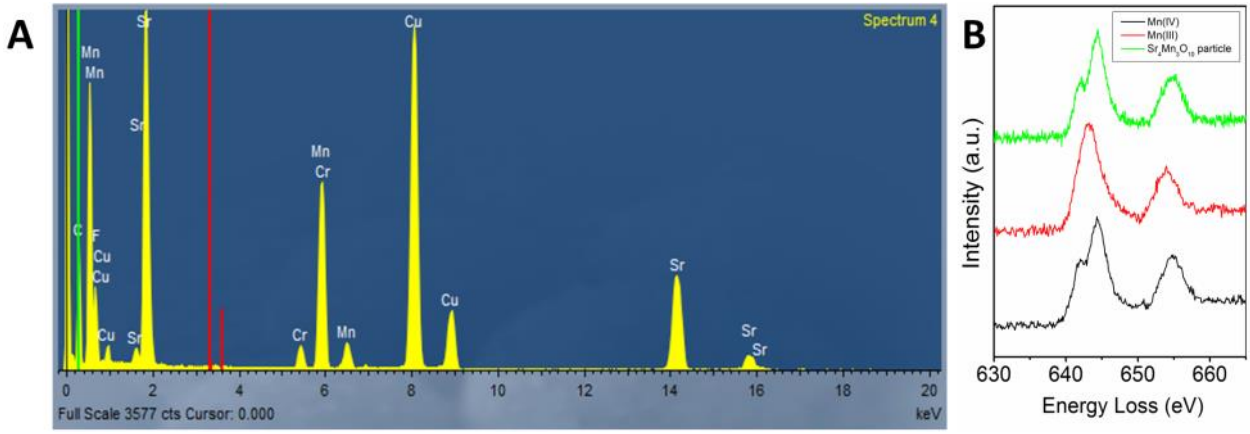

Figure S5. Analytical TEM analysis of unwashed $Sr_4Mn_3O_{10}$ platelets obtained after 1 h of heat treatment. (A) EDX and (B) EELS analyses of unwashed particles within the quenched reaction medium. In A, the C and Cu signals come from the grid, the Cr signal comes from the sample holder. The red bars in A indicate the position of the K-α lines of potassium, which is absent from the spectrum and then can be ruled out as potential impurity that would have come from the $KMnO_4$ reagent. The black and red EELS spectra in B are spectra of reference Mn^{4+} and Mn^{3+} species. The $Sr_4Mn_3O_{10}$ particles (green) are solely made of Mn^{4+}. Altogether, EDX and EELS show that the unwashed particles are pure $Sr_4Mn_3O_{10}$.

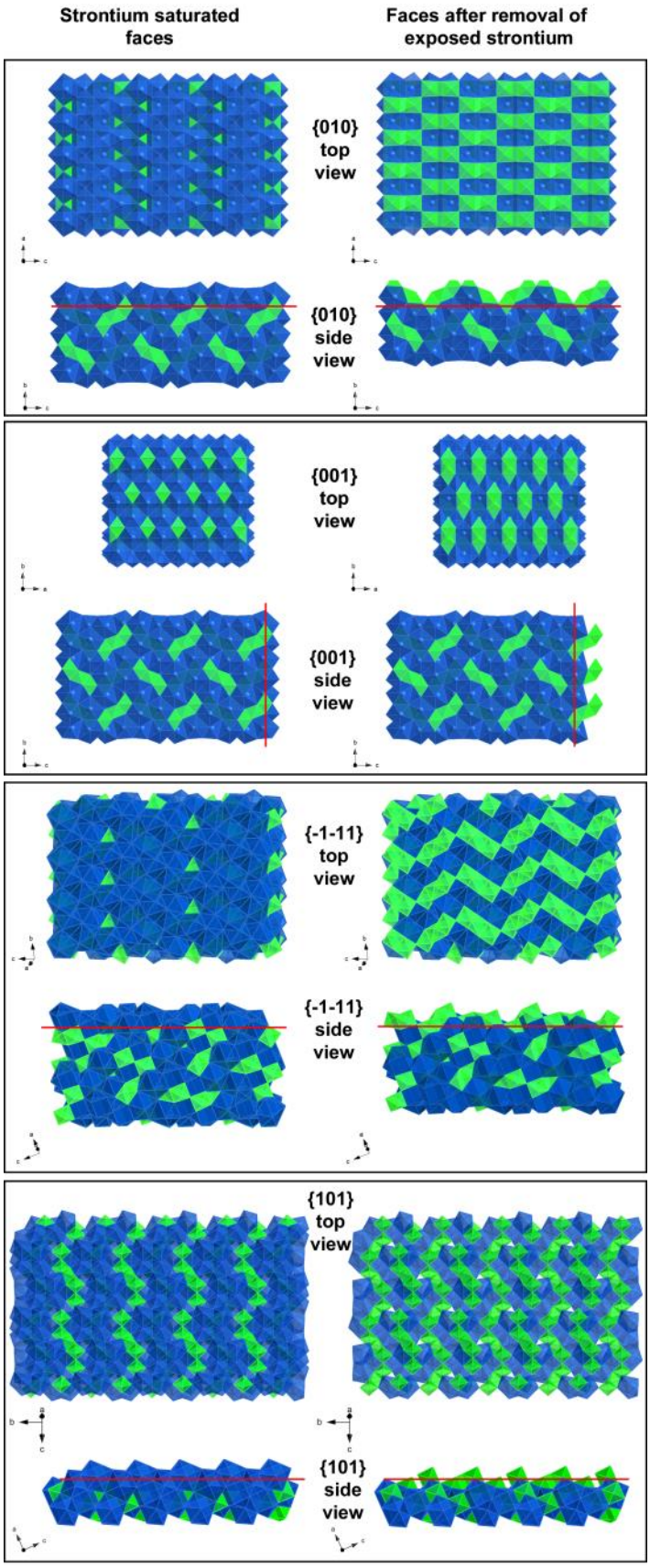

Figure S6. Exposed faces of primary particles: {010}, {001}, {-1-11}, {101} facets. MnO_6 and SrO_{10} polyhedra are pictured in green and blue, respectively. Top and side views. Left column shows most Sr-enriched slabs of each plane. Those correspond to the most probable composition of exposed facets in molten strontium hydroxide. Right column shows after removal of the Sr^{2+} cations exposed in the configuration of the left column.

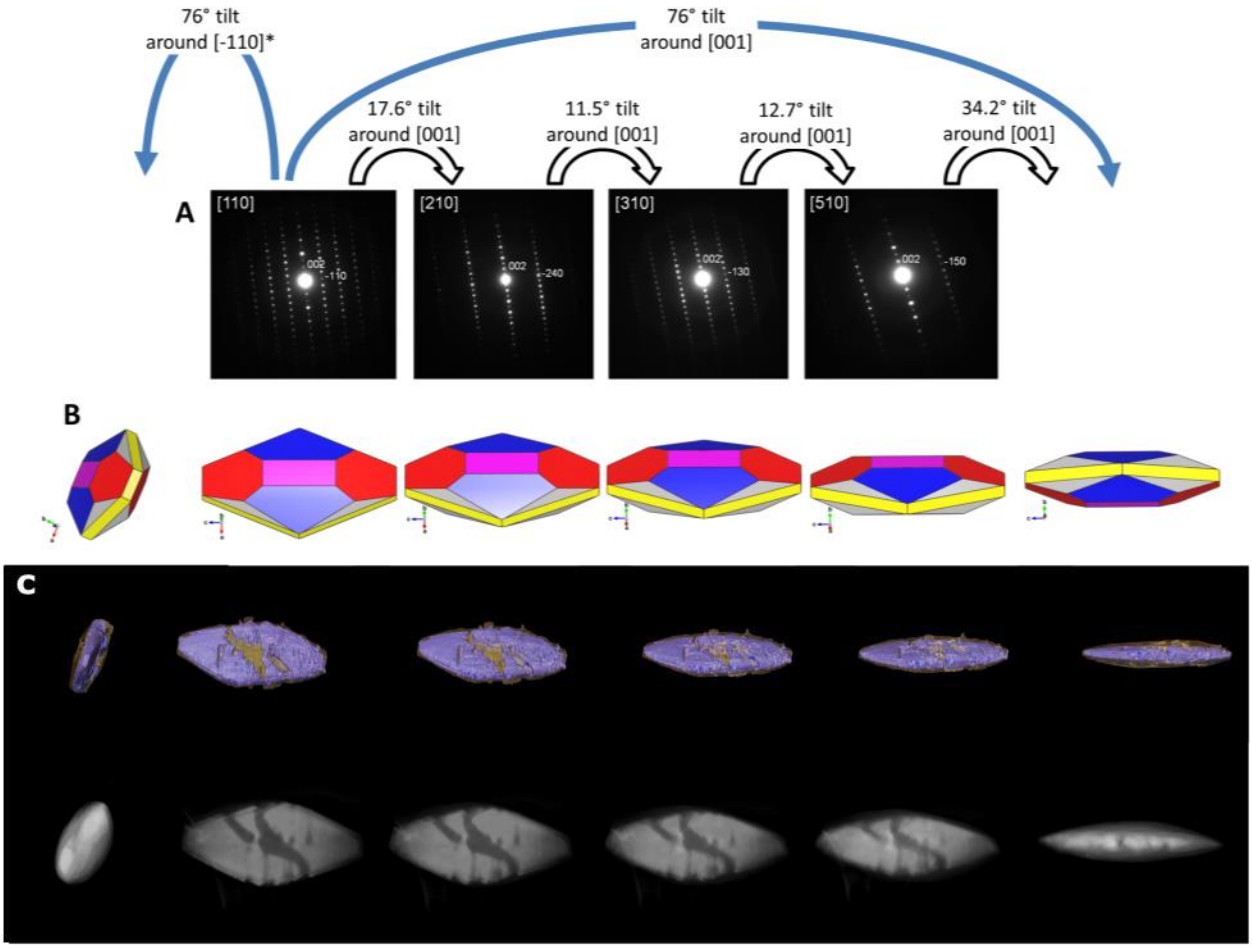

Figure S7. Tilt series acquired on a $Sr_4Mn_3O_{10}$ platelet from a sample washed after 72h of heat treatment. (A) SAED patterns; (B) corresponding projections from the morphological model and projections at the maximum experimental tilt angle of 76° around the [-110]* and [001] axes; (C) corresponding experimental projections from the STEM-HAADF tomography reconstruction.

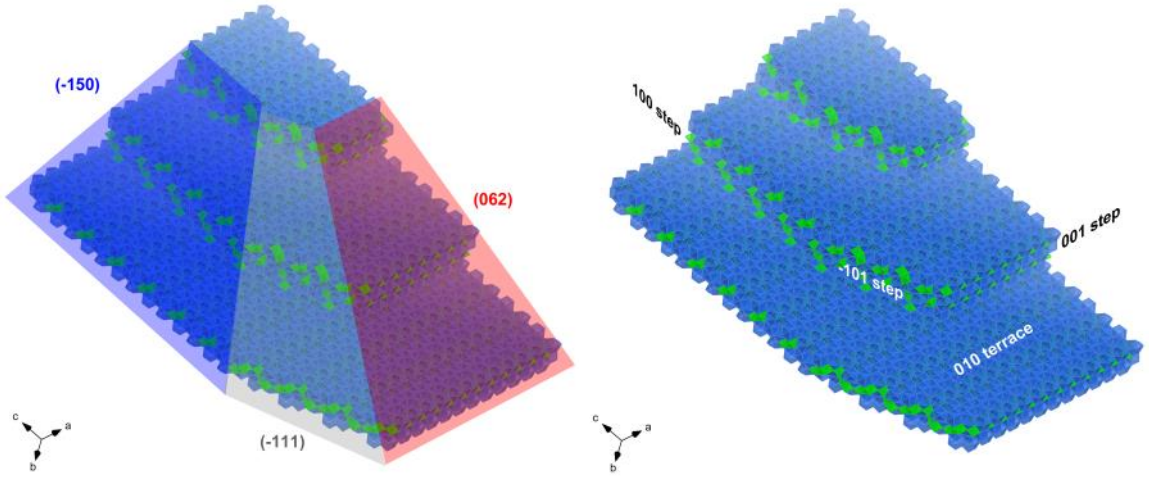

Figure S8. The basal face ({150}, {111}, {062}) of $Sr_4Mn_3O_{10}$ platelets: interpretation as (001), (100), (101)-stepwise (010) face with the most Sr-enriched configuration. MnO_6 and SrO_{10} polyhedra are pictured in green and blue, respectively.

MUSIC^2 model

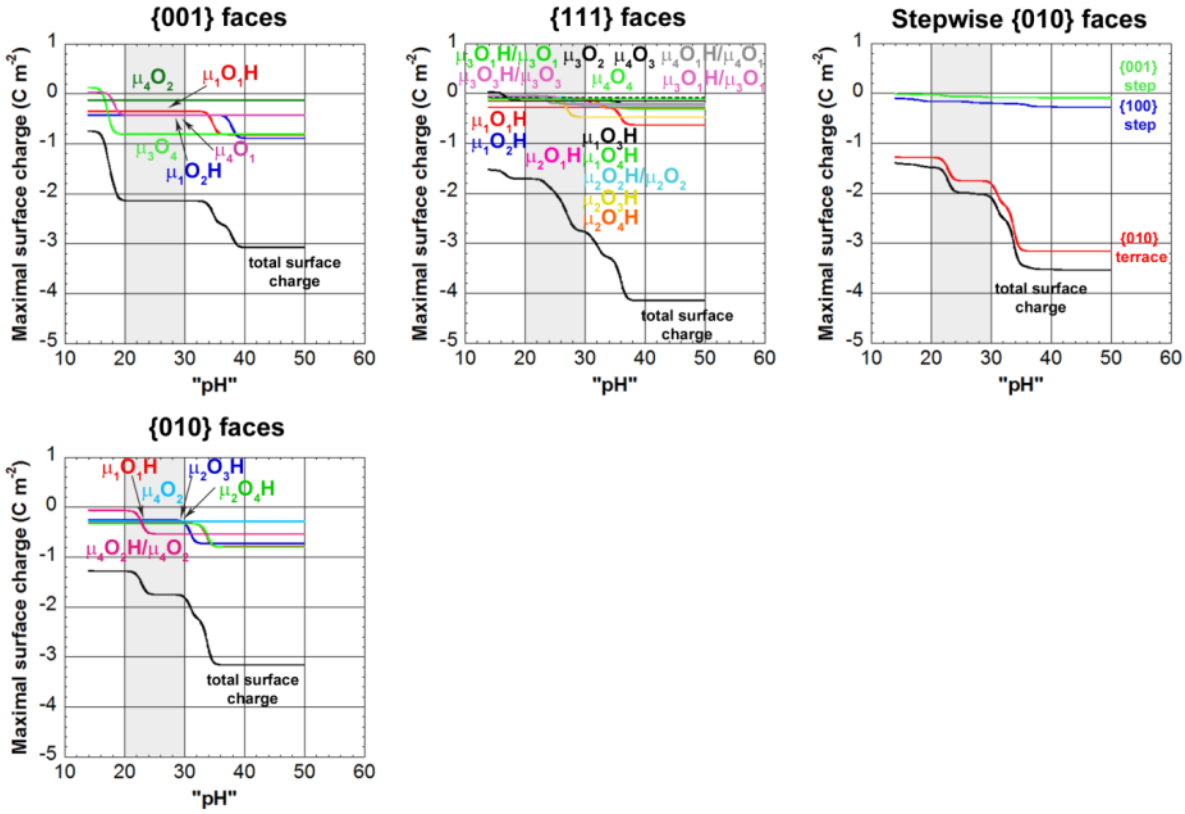

Figure S9. Maximal surface charges evaluated according to the MUSIC^2 model. See the "methods" section for the significance of "pH" in the molten hydroxide medium. The grey area is the most probable area corresponding to experimental conditions of particles growth. In the synthesis conditions (**SI**), {001} and {111} faces possess similar surface charge while stepwise {010} basal faces exhibit the lowest charge. Note that the occurrence of steps does not change significantly the charge of the basal face, so that eventual {101} steps (**Figure S9**) are omitted.

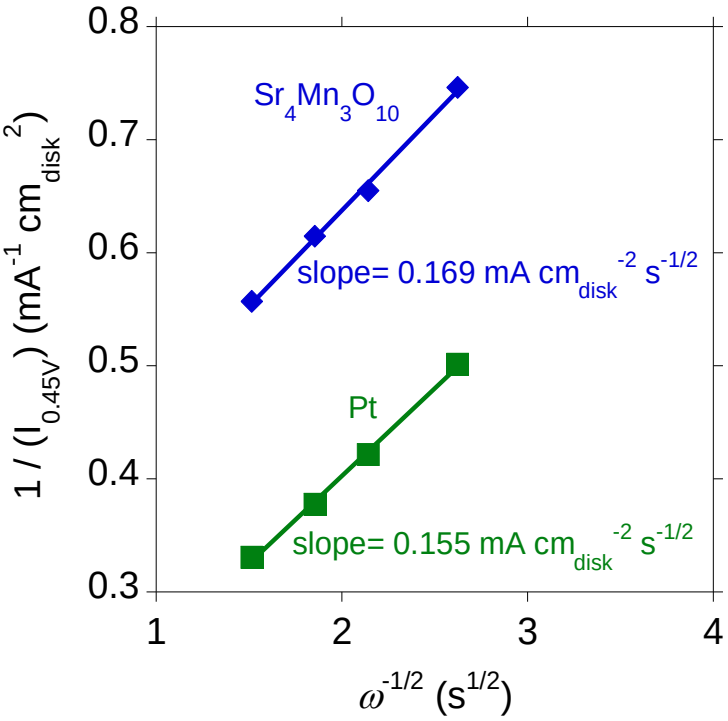

Figure S10. Koutecky-Levich plots for the oxygen reduction reaction on commercial Pt/C catalyst and on $Sr_4Mn_3O_{10}$. The slope is inversely proportional to the number of electrons involved in the reaction. The multiplication factor is independent of the catalyst, so that parallel lines indicate the same number of involved electrons (J. Suntivich, H. A. Gasteiger, N. Yabuuchi, Y. Shao-Horn, *J. Electrochem. Soc.* **2010**, *157*, B1263). Pt is known to undergo ORR by a 4 electrons reduction down to water and used as a normalizing sample. The resulting number of electrons exchanged for $Sr_4Mn_3O_{10}$ is 3.7

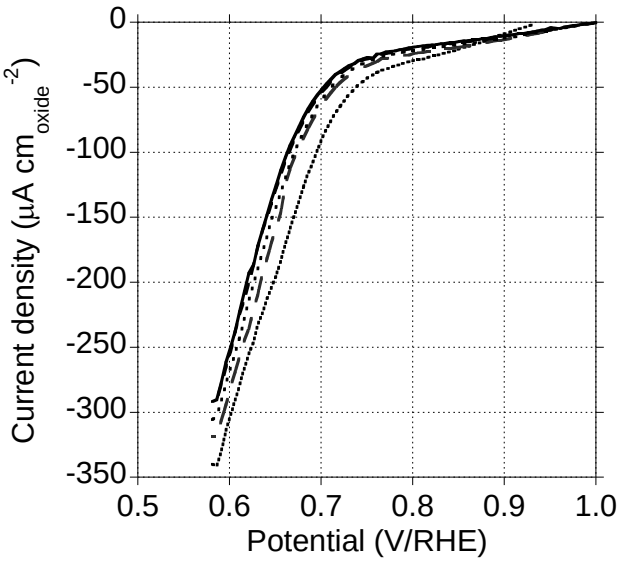

Figure S11. First 5th voltametric cycles (corrected from capacitive current) of $Sr_4Mn_3O_{10}$. After 3 cycles, the current density stabilizes at ~-280 μA cm^{-2}_{oxide}

TABLES

Table S1. Energy loss (eV) of the Mn-$L_{2,3}$ edges for $Ca_2Mn_3O_8$, $LaMnO_3$, $Ca_2Mn_3O_5$ and $Sr_4Mn_3O_{10}$.

Sample	E (eV) Mn-L_3	E (eV) Mn-L_2
Crystalline area $Sr_4Mn_3O_{10}$	644.4	654.9
Amorphous area $Sr_4Mn_3O_{10}$	641.9	653.6
$Ca_2Mn^{4+}{}_3O_8$	644.4	654.9
$LaMn^{3+}O_3$	643.2	654.0
$Ca_2Mn^{2+}{}_3O_5$	641.2	652.3

Mn-$L_{2,3}$ EELS spectra corresponding to standards as well as crystalline and amorphous areas of $Sr_4Mn_3O_{10}$ are shown in **Figure 1L.** The corresponding Mn-$L_{2,3}$ energy loss values are summarised in **Table S1.** In the crystalline areas, the high energy resolution achieved allows observing the splitting of the Mn-L_3 line in agreement with calculated octahedral environment Mn^{4+} spectrum [G. Radtke, C. Maunders, S. Lazar, F.M.F. de Groot, J. Etheridge, G.A. Botton, "The role of Mn in the electronic structure of $Ba_3Ti_2MnO_9$" *Journal of Solid State Chemistry*, 178 (2005) 3436–3440]. The energy of both L_3 (644.4 eV) and L_2 (654.9 eV) white lines are in agreement with those exhibited by Mn^{4+} in $Ca_2Mn_3O_8$ confirming that Mn is only present as Mn^{4+} in the crystalline zones of the $Sr_4Mn_3O_{10}$ particles. However, when the analysis is performed on the amorphous areas, the shift of the Mn-$L_{2,3}$ edge towards lower energies indicates a higher concentration of manganese in lower oxidation state in agreement with the observed Sr depletion in order to balance electroneutrality.